Wet electrospinning-aided self-assembly of multifunctional GO-CNT@PCL core-shell nanocomposites with spider leg bioinspired hierarchical architectures

Roberto Scaffaro*, Michele Gammino, Andrea Maio*

Department of Engineering, University of Palermo, Viale delle Scienze, ed. 6, 90128 Palermo (Italy).

*Corresponding authors: roberto.scaffaro@unipa.it; andrea.maio@unipa.it

Abstract

We report a fast route enabling the multiscale design of nanohybrid structures comprising a 3D fibrous network of polycaprolactone (PCL) wrapped by graphene oxide (GO) sheets onto which carbon nanotube (CNT) brushes are anchored. The method relies on electrospinning PCL solutions onto a suspension of GO and CNTs in ethanol. Self-assembly is due to electrostatic wrapping of GO sheets around PCL fibers and π-π stacking between GO and CNTs. Hierarchical architecture and nanopatterned surface allow gathering the starting properties of PCL, GO and CNTs into lightweight (99% porosity) yet robust (1575% stiffness improvement), amphiphilic monoliths that can remove methylene blue and/or methyl orange from stagnant water with ca.100% efficiency.

Keywords: A. Carbon nanotubes; A. Graphene and other 2D-materials; A. Hybrid composites; B. Multifunctional properties; E. Electro-spinning.

1. Introduction

The simultaneous removal and recovery of chemical contaminants from water is of crucial importance to enhance the supply of safe drinking and clean water, while allowing the reuse of chemical compounds, in compliance with circular economy and zero-waste guidelines[1–8]. With the rapid growing of this field, more efficient fabrication and modification strategies have been developed, based on the manipulation and combination of a wide variety of materials and nanotechnologies, each one with its own advantages and disadvantages. Basically, absorbent materials must meet many prerequisites, the optimization of which requires a multidisciplinary approach, which encompasses knowledge of various fields, including processing (nano)technology and surface engineering. For instance, surface area and properties directly govern the adsorption capacity and mechanism. Hence, adequate levels of porosity, surface area and roughness, along with tailored wettability, are crucial to allow efficient removal [2]. Meanwhile, mechanical robustness should be high enough to make these devices capable of withstanding severe external stresses, such as use in turbulent flow conditions or being squeezed or even reused, without losing fragments that would cause secondary pollution [9]. Indeed, turbulence is often necessary in the adsorption processes due to the poor wettability of the proposed systems, with evident repercussions on costs and applicability, while the possibility of treating wastewater in the absence of stirring and pH or temperature regulation, could significantly increase the eco-sustainability of the overall process. In addition to this, the next generation of sorbents should be prepared using cleaner techniques, i.e. with fewer production steps and without the use of hazardous/toxic chemicals. Several nanomaterials, including metal organic frameworks (MOFs), nanoclays and especially carbon nanotubes (CNTs) and graphene or graphene oxide (GO), showed excellent sorption performances, owing to their extended surface area and affinity to various contaminants [2,8,10–13]. Despite this, their difficulty to be handled and removed from water motivated the necessity to incorporate or anchor them into various substrates with well-defined morphology. Aerogels based on graphene and/or CNTs proved to be particularly promising for removing both anionic and cationic dyes [2], while conversely displaying some disadvantages related to their limited mechanical robustness, and time-consuming manufacturing processes, which involve at least chemical coupling followed by freeze-drying, and in some cases even post-synthesis treatments [14,15]. On the other hand, the preparation of porous core-shell nanocomposites, having a flexible polymeric skeleton coated with GO-CNTs as active compounds, offers the possibility to conjugate the easy processability and good mechanical properties of polymers with the adsorption performance ensured by the surface characteristics of external sheath. Unfortunately, the protocols currently adopted involve multi-step procedures, whose laboriousness increases as the morphological and functional complexity of hierarchical structures increases. Basically, all these approaches include the fabrication of a porous substrate, generally performed by freeze drying, electrospinning, pressure gyration, or centrifugal spinning, and the subsequent surface engineering, accomplished by either spin coating, dip coating, spray coating, CVD, electrophoretic deposition, or mussel-inspired chemistry, that must be performed after substrate fabrication [16–21]. Hence, the aim of this work is to explore the feasibility of preparing multifunctional structures, by electrospinning polycaprolactone (PCL) solutions onto an active liquid collector made of colloidal suspensions of GO and CNTs in ethanol. In fact, once the features of nanoparticles are suitable to ensure a peculiar self-assembly with polymeric fibres that sink into the bath, such technique might enable the ultrafast fabrication of porous polymeric materials coated with a hybrid GO-CNT framework. Moreover, we analyzed mechanical performance and surface characteristics of such materials, along with the possibility to perform an energy-saving removal of anionic and/or cationic dyes from wastewater, to assess whether the assembled networks own emerging functions exceeding the sum of the properties of the individual components [21–23].

2. Experimental section

2.1 Materials and preparation methods

PCL (M_n = 80 kDa, $M_w/M_n < 2$, density = 1.14 g/cm^3, melting temperature = 60 °C), dichloromethane (DCM), ethanol (EtOH), deionized distilled water (DDW), acetone, methylene blue (MB), and methyl orange (MO) were purchased by Sigma-Aldrich. All the reactants were ACS grade and used without any further treatment. GO (lateral size < 45 µm, thickness = 0.7-0.8 nm, C/O ratio=1.1, density = 1.76 g/cm^3) and MWCNTs (length =1-2 µm, diameter=10-20 nm, C/O ratio=40.7, density = 2.24 g/cm^3) used in this study were synthesized by our group and further details about synthetic routes adopted and physicochemical characteristics can be found in our previous works [9,24–27]. For the preparation of the fluffy scaffolds, we designed a vertical electrospinning setup equipped with a stirred coagulation bath, acting as a liquid collector (**Figure 1**). PCL (10 wt. %) was dissolved in DCM/EtOH (3:1 by volume) solvent mixture under stirring and then loaded (10 mL) to a glass syringe equipped with a 19G stainless steel needle (diameter = 0.8 mm). Dry jet wet electrospinning was conducted by keeping constant the following operating parameters: voltage (17 kV), flow rate (1.19 mL/h), dry jet height (12 cm), liquid height (2.5 cm), and processing time (3 min), optimized in a previous work [9]. As illustrated in **Table 1**, four different samples were therefore fabricated by changing solely the composition of coagulation bath, whose conductivity and surface tension are provided in the same table. Of course, the wet fluffy coming from this process can be dry formed to achieve the desired shape. In this work, cylindrical specimens (*D* = 4 mm, height = 5.5 mm) for each sample were obtained by using a 48-cylindrical mould plate and subsequently left to dry at room temperature.

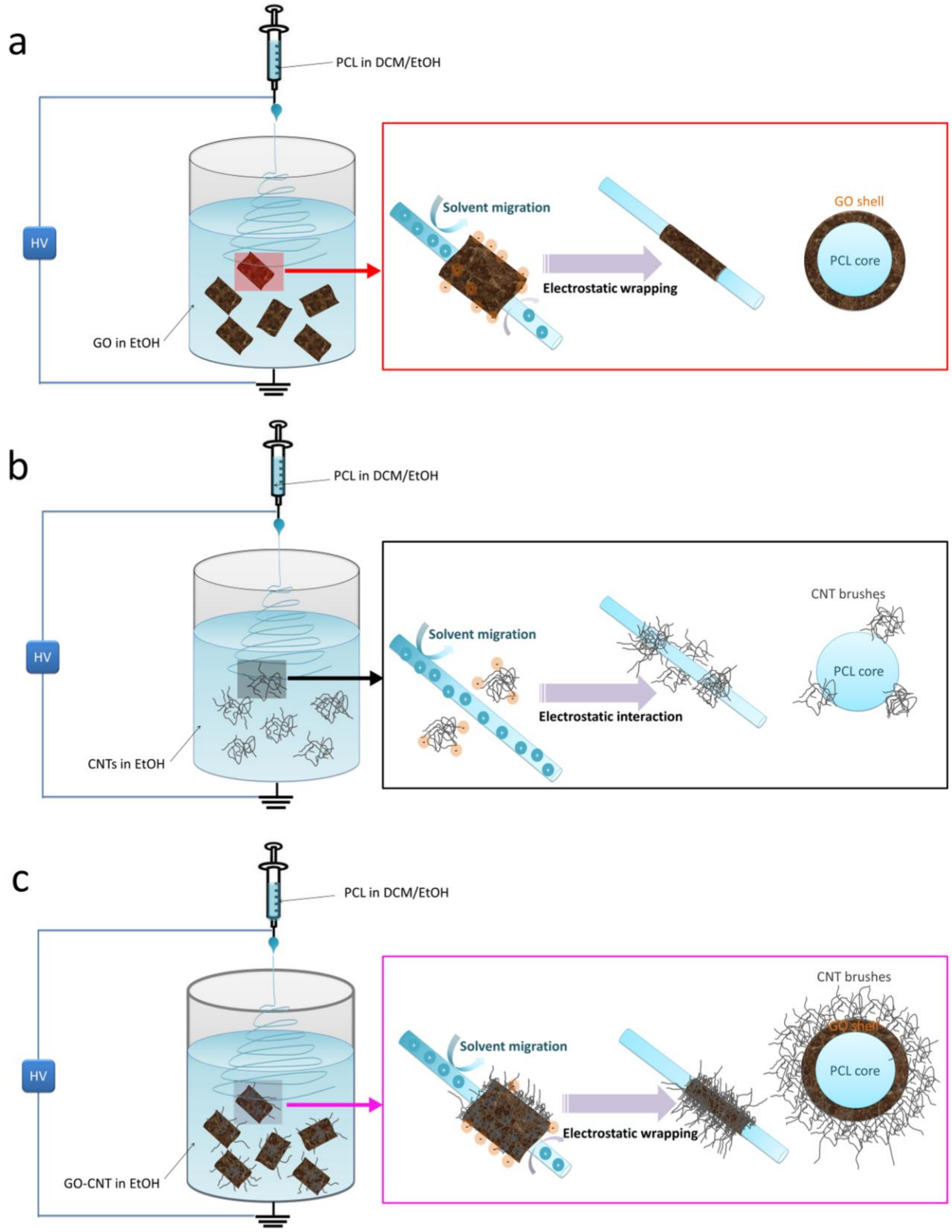

Figure 1. Pictorial description of *in situ* decoration during wet electrospinning to obtain GO@PCL (a), CNT@PCL (b), and GO-CNT@PCL (c).

Table 1. Samples prepared varying composition of coagulation bath.

	Coagulation bath		
Sample	Composition of EtOH bath	Surface tension	Electrical

	GO (mg/L)	CNT (mg/L)	(mN/m)	conductivity (µS/cm)
PCL	-	-	27.3	0.7
GO@PCL	0.5	-	28.1	19.9
CNT@ PCL	-	0.15	27.6	44.5
GO-CNT@PCL	0.5	0.15	28.6	29.3

2.2 Characterizations

Attenuated total reflection Fourier transform infrared (FT-IR/ATR) measurements were performed by using a FT-IR/NIR Spectrum 400 spectrophotometer (PerkinElmer) in the range 4000–450 cm^{-1}. Micro-Raman spectroscopy was carried out in the range 1000–2000 cm^{-1} by means of a Renishaw InVia instrument (Renishaw) with diode laser excitation at 633 nm and spectral resolution equal to 1 cm^{-1}. For each sample, at least ten measurements have been collected on different specimen positions. Curves were multi-peak fitted by means of Lorentzian (R^2>0.999; $\chi^2<5*10^{-4}$). Wide angle X-ray diffractometry (WAXD) analysis was conducted by means of an Empyrean PANalytical II diffractometer with a Cu Kα radiation source (λ = 1.5406 Å). Scanning electron microscopy (SEM) imaging was performed by using an ESEM FEI QUANTA 200 microscope (Thermo Fisher Scientific). Fibre diameter distribution was determined using ImageJ software, equipped with Diameter J plug-in. Atomic force microscopy (AFM) measurements were performed in air using a Bruker FAST-SCAN microscope equipped with a closed-loop scanner, in the soft tapping mode using a probe with an apical radius of about 5 nm. Arithmetic average roughness (Ra) and quadratic mean roughness (Rq) were calculated on squared areas (side length=600 nm). The overall nanoparticle content and porosity of core-shell scaffolds were calculated by helium pycnometry, which allows measuring both skeletal and apparent densities of the samples. More details about this procedure can be found in our previous work[9] and in SI. Specific surface areas were measured according to the Brunauer–Emmet–Teller (BET) method from the N_2 adsorption data by using a Micromeritics ASAP 2020. Mechanical tests in compression mode were performed in both air and water by means of a dynamometer (Instron 3365, U.K.) equipped with a 1 kN load cell and a BioPuls Bath (Norwood, USA), until specimen failure by imposing a uniform strain rate of 1 mm min^{-1}. Data were analyzed to determine elastic modulus in the linear region, calculated as the slope extrapolated at zero strain, and in the densification region, by measuring the slope of each stress–strain curve after yielding point. This latter was calculated as the intersection of the two tangent lines to the curve in the linear and in the densification regions. Water contact angle (WCA) testing was performed at room temperature by using an FTA 1000 (First Ten Ångstroms, U.K.) instrument. Four µL of deionized water were dropped onto the surface of each sample by way of an automatic liquid drop dosing system. Images of the drops onto the surface were acquired in the time range from 0.033 to 300 s. For sorption tests, aqueous solutions of Methylene Blue (MB) (0.5 mM) and Methyl Orange (MO) (0.1 mM) were prepared. For each experimental run, 6 scaffolds (approximately 60 mg) were immersed into 50 mL of solution; the sorption capacity of samples was assessed by monitoring at predetermined time intervals the residual pollutant concentration via UV–vis spectroscopy, carried out in a UV–vis Specord 252 spectrophotometer (Analytik Jena, Jena, Germany). Absorbance values of the characteristic signals were converted into concentrations by using opportunely constructed calibration lines (Fig. S1). Initial concentrations of pollutants were then chosen on the basis of readability of absorbance, i.e., as the maximum value before saturation. Sorption tests were conducted in the total absence of stirring, that is, in the most critical conditions, since it is well-known that the rapidity of sorption process increases upon increasing the stirring rate, due to the positive hydrodynamic influence especially in the case of turbulent flow [28]. The time-dependent sorption capacity of materials, Q_t, and removal efficiency (%) were evaluated by using the following equations (Eqn. 1-2):

$$Q_t = \left(\frac{C_0 - C_t}{m_{sorbent}}\right) V \qquad (1)$$

$$Removal\ efficiency\ (\%) = \left(\frac{C_0 - C_t}{C_0}\right) \times 100 \qquad (2)$$

3. Results and discussion

Figure 2 reports SEM micrographs of PCL, GO@PCL, CNT@PCL, and GO-CNT@PCL. All the samples show a three-dimensional fibrous architecture, which can be governed by controlling some characteristics of coagulation bath. In fact, using ethanol as a non-solvent allows the polymeric fibres to sink, because it has density lower than PCL and sufficiently low surface tension (ca. 20 mN/m).

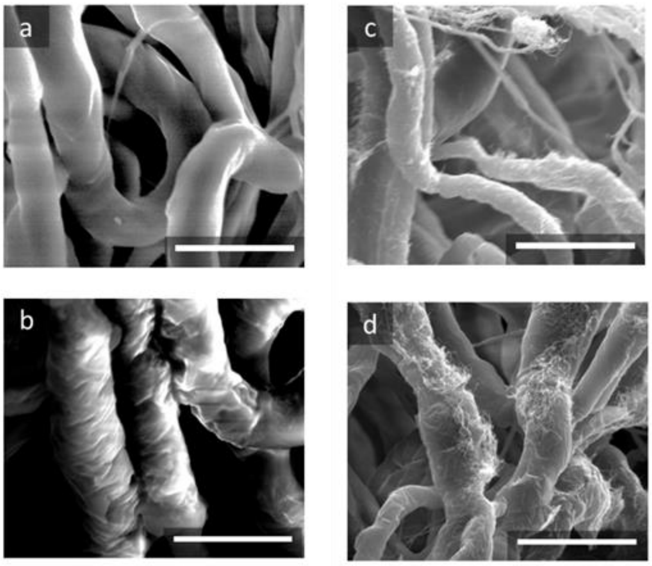

Figure 2. SEM micrographs of PCL (a), GO@PCL (b), CNT@PCL (c) and GO-CNT@PCL (d). Scale bar: 5 µm.

As the fibres dip into bath, their morphology is frozen by the rapid solvent migration from the polymer to liquid phase, while their spatial arrangement is determined by the flow-induced memory, which depends on stirring. At a microscale level, the quality of fibres, that is, the absence of beads and blobs, as well as their mean diameter, can be a priori designed through the appropriate optimization of electrospinning parameters and viscosity of polymeric solution, which is obviously the same for all the samples. The different compositions of coagulation bath, intended as type and content of nanoparticles suspended in ethanol, were instead used to obtain different types of fibre coatings. Therefore, all the prepared materials have similar macro- and micro-scale architectures, while differing each other for their nanoarchitecture, i.e., surface topochemistry. In this latter regard, it is worth noting that GO@PCL and GO-CNT@ PCL showed uniform coating, while CNT@PCL exhibited a discrete amount of nanoparticle decoration. To explain the different features of such coatings, it is worth highlighting that GO, owing to its high content of oxygenated moieties, can form quite stable dispersions in ethanol, whereas CNTs, bearing fewer carbonyl and alcohol moieties mainly located onto their tips, organize themselves into bundles, due to Van der Waals forces and Brownian motions, and their dispersion is known to reveal an optical anisotropy induced by electric field [29,30]. The hybrid suspensions of GO and CNTs in ethanol displayed a substantially homogeneous dispersion, likely due to the unique feature of GO that can interact with both CNTs and EtOH solvent, respectively exploiting aromatic domains and oxygenated groups of its double honeycomb. **Fig. S2** reports diameter distributions of fibres in the four samples (a-d) and mean diameters plotted as a function of electrical conductivity of the coagulation bath (e). Indeed, the presence of GO and/or CNTs in the coagulation bath may have at least two opposite repercussions on size distribution and mean diameter. On one hand, the formation of a nanoparticle outer shell is obviously supposed to cause thickening of PCL fibres. On the other hand, the enhanced electrical conductivity of the coagulation bath (see Table 1) in the presence of electroactive nanoparticles is known to promote the formation of thinner fibres with narrower size distributions. CNT@PCL showed the thinnest fibres, with almost half of them having submicrometric diameter, relying on the highest conductivity of the bath and on the discrete nanoparticle decoration, followed by GO-CNT@PCL. Notably, GO@PCL displayed the highest mean diameter, however similar to that of PCL, albeit a bath conductivity 20 times higher. This aspect could be due to the formation of a thick GO-coating, thus counterbalancing the shrinking effect induced by the higher electrical conductivity. Filler content and porosity of the scaffolds were estimated by pycnometric density measurements according to Eqns. S1-S4 (see SI).

Table 2. Filler content and porosity of the scaffolds prepared, assessed by Eqns. S1-S4 (see SI)

Sample	filler content(wt.%)	filler content (vol.%)	porosity (%)
PCL	-	-	98
GO@PCL	33	24	96.5
CNT@PCL	36.5	23	98.5
GO-CNT@PCL	~63	~50	98.9

The results, provided in **Table 2**, show that this preparation route allows decorating PCL fibrous fluffs with an outstanding content of nanoparticles. Moreover, the porosity levels attained are approximately 96-99%, i.e., slightly lower than those of aerogels but quite higher than those of sponges and foams. The type of fiber decoration might greatly affect roughness and surface area. The results of the AFM measurements are shown in **Figure 3**, in which both 2D views (top panels) and 3D views (bottom panels) are provided, with the latter highlighting the texture of the areas on which the roughness has been calculated in terms of arithmetic (R_a) and quadratic mean (R_q). The outcomes confirm what was already qualitatively observed in the SEM analysis. PCL fibers have a smooth surface, while after decoration with CNT, GO, and GO-CNT, the roughness increases by 6, 12 and 15 times, respectively. The highest values of R_q and R_a showed by hybrid coating, presumably arise from the synergistic combination of the wrinkled texture of both nanoparticles and spider leg-like configuration of fibers, with a uniform and dense forest of aligned CNTs planted on GO layers. By contrast, the heterogeneous decoration of CNT@PCL, bearing scarcely decorated zones (zone 1) and densely decorated CNT forests (zone 2), resulted in the lowest value of roughness among the nanocomposites, yet higher than neat polymer.

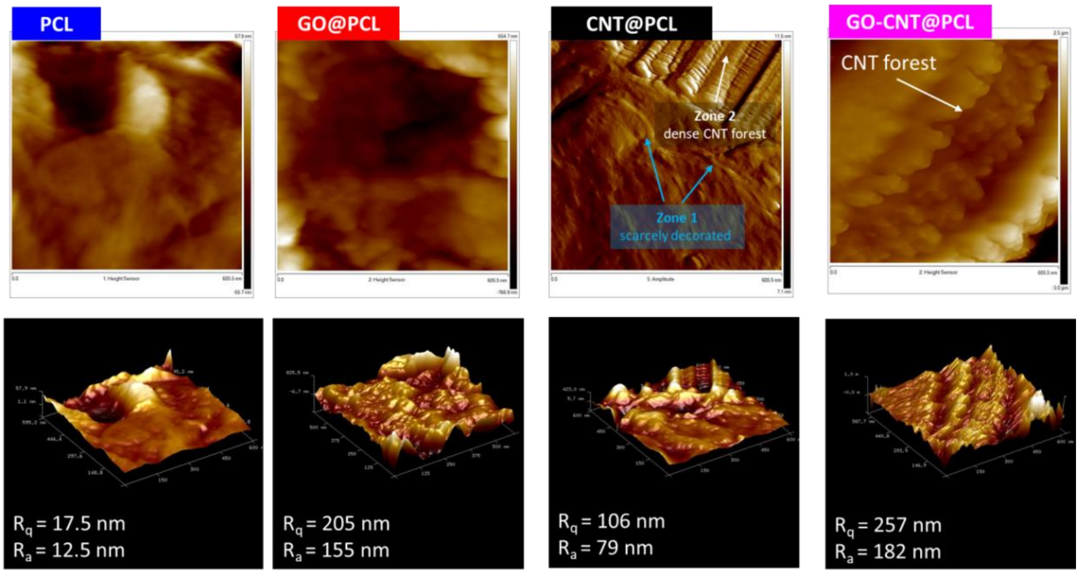

Figure 3. AFM analysis: 2D views (top panels) and 3D views (bottom panels) of the areas selected for the calculation of R_q and R_a

The results of specific surface area (SSA) analysis are provided in **Figure S3**. While the uncoated scaffolds display SSA as low as 2.16 m^2/g, the coated samples experience an outstanding increase, with SSAs equal to 8.01, 4.87 and 12.07 m^2/g, respectively for GO@PCL, CNT@PCL, and GO-CNT@PCL. Again, hybrid coating gave the best results, even higher than the sum of the two single coatings, likely due to the effect of spider leg-like architecture and submicrometric pores. Indeed, the adsorption/desorption isotherms of coated materials show hysteresis loop at different yet high values of relative pressure, indicating the existence of micro-, meso- and macropores, although at a different extent and proportions depending on the type of coating. The pore size distribution confirms the presence of pores within the range 0.1–300 nm for all the coated systems, with similar values of average width (48-52 nm) but different volume, which proved to be equal to 0.11, 0.05, and 0.14 cm^3/g for GO@PCL, CNT@PCL, and GO-CNT@PCL, respectively.

The effect of nanoparticle decoration on the structural features of PCL-based fluffy scaffolds was studied by FTIR, μ-Raman, and WAXD. Because of the scarce IR-activity of carbonaceous materials, FTIR spectra (**Fig. S4** a-d) proved to be more suitable to detect key-bands of PCL, while those of GO were scarcely recognizable, except for the broad band in the range 3600-3000 cm^{-1}, and a shoulder located at ca. 1640 cm^{-1}, respectively ascribed to –OH stretching and C=C sp^2 framework of GO (see close-up of panels b-c). Notably, once CNTs are planted onto GO foils, both modes were found to disappear. PCL retains all its features after decoration, albeit the mutual intensity ratio of the modes centred at 1190 cm^{-1} (ν_s(OC—O)) and 1260 cm^{-1} (ν_{as}(C—O—C)), proved to overturn after decoration (Fig. S4 d), thus suggesting some interaction between ester groups of PCL and oxygenated moieties of GO. μ-Raman spectroscopy was used to analyze the carbonaceous counterpart of materials. **Figure 4** provides spectra of GO@PCL (a), CNT@PCL (b) and GO-CNT@PCL (c), along with those of starting components. Due to the apparent similarity in the spectral features of materials containing GO and/or CNTs, curves were multi-peak fitted. This analysis enabled us to detect not only the well-known D (symmetry out-of-plane A_{1g} mode) and G (E_{2g} mode of sp^2 carbon atoms) bands, but even the satellite and inter-bands caused by the activation of modes arising from multiple defects, curvature, small sized aromatic domains, and oxygenated moieties, which are peculiar of each nanocarbon material [31–36]. The main assignments are reported in **Table S1**, based on literature data [35–39]. Consistently with morphological results, μ-Raman mapping highlighted that GO@PCL and GO-CNT@PCL display homogeneous spectra in different zones, whereas

CNT@PCL displayed two different “families” of spectra, labeled as zone 1 and zone 2, respectively indicating scarcely and densely decorated fibres.

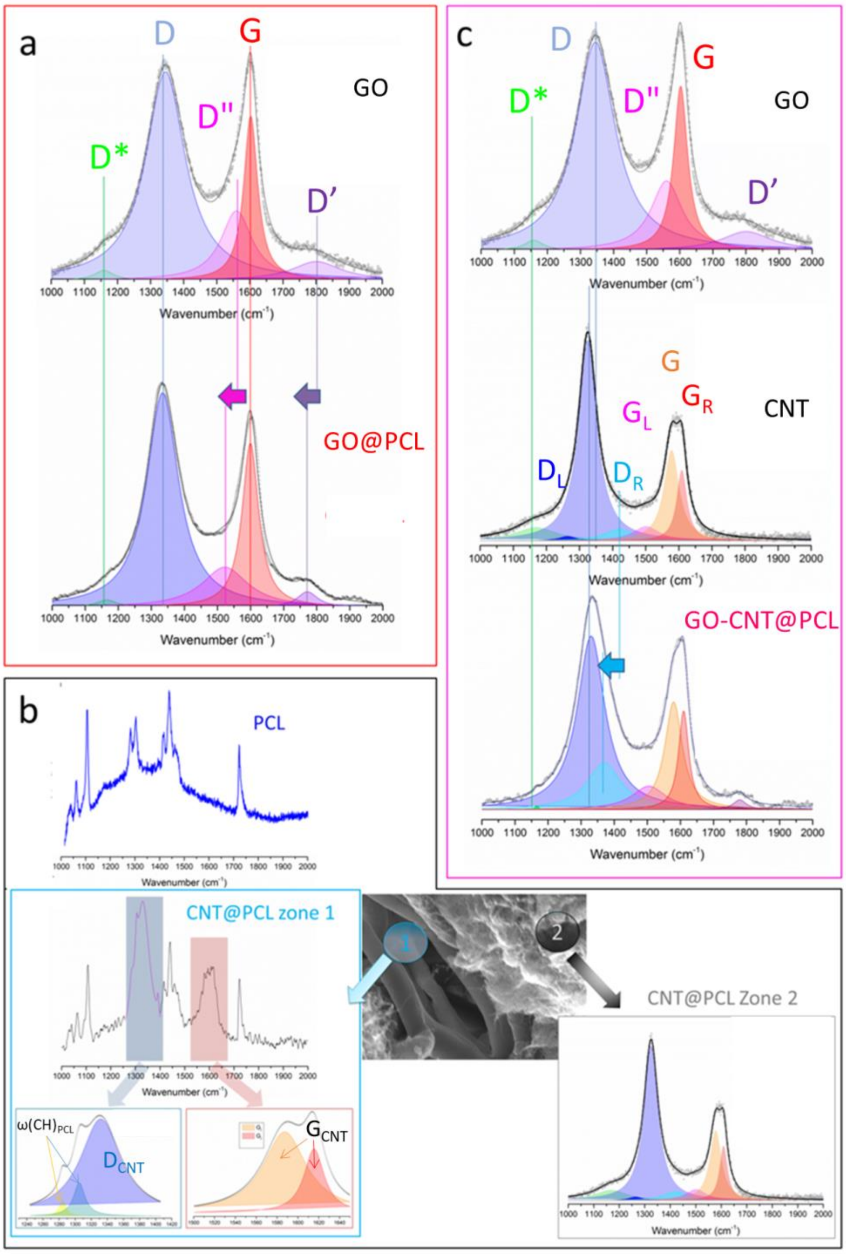

Figure 4. Raman spectra of GO@PCL (a), CNT@PCL (b), GO-CNT@PCL together with those of starting components for sake of comparison.

The former shows main peaks of both PCL and CNTs, while the latter is very close to that of CNTs. GO@PCL spectrum (Fig. 3a) is dominated by the features of GO, although the partial suppression and the eventual downshift of the modes D*, D” and D’, respectively located at 1160, 1560, and 1775 cm^{-1}, likely indicate either a tensional state induced by underlying PCL substrate, or a further distortion of oxygenated sub-lattice of GO lamellae interacting with the polymer. In GO-CNT@PCL, Fig. 3c, Raman spectrum proved to be mainly governed by CNTs, while GO modes are scarcely visible and PCL ones are not detected. This aspect, in full agreement with the outcomes of AFM analysis, testifies the formation of a unique spider leg-like hierarchical architecture, with CNTs forest planted onto surface of GO lamellae, which in turn wrap the underlying PCL. In details, some typical modes of CNTs (D, G_L, G and G_R) retain their peak positions and shapes, while mutual intensity ratios proved to be a linear combination of those of CNTs and GO. The presence of this latter is confirmed by the peculiar D' mode at 1775 cm^{-1}. The main variations attributable to the formation of a hybrid GO-CNTs framework are the suppression of the D* modes (1160-1165 cm^{-1}) of both nanoparticles and the insurgence of a mode centred at 1370 cm^{-1}, likely due to the combination of D_R of CNTs and D band of GO. WAXD analysis was carried out to perform a bulk analysis of such structures. The results **(Fig. S5)** indicate that crystalline forms of PCL are still preserved after decoration, as indicated by the diffraction peaks at 20.5° and 24.5°, along with the shoulder at 21.2°, respectively attributable to (110), (200), (111) planes. The presence of GO is well-detectable in both GO@PCL and GO-CNT@PCL, although the typical (001) peak at 8.7° was found to upshift to – respectively – 9° and 9.5°, indicating a contraction of interlayer distance after wrapping. On the other hand, the CNT peak ($2\theta = 26°$) is scarcely visible after decoration, being individuated as a weak shoulder (see right panel of **Fig. S5**). Mechanical performance of samples was evaluated by compressive tests. **Figure 5** shows the representative stress-strain curves of materials. For each curve it is possible to recognize three distinct portions, respectively representative of initial linear (I), transition (II), and densification (III) regions. (I) and (III) show linear variations of stress as a function of strain, respectively indicating the initial compression of pores and the bulk resistance toward compression of samples, once every pore is collapsed. Analysis of curves was focused on deriving some salient properties (see Tab. 3), including elastic moduli in the two linear regions, respectively indicated as E_I and E_{III}, along with yield strain ($\varepsilon_{Y,II}$) and stress ($\sigma_{Y,II}$), detectable in zone II, graphically calculated as the intersection of the two straight lines, and maximum strength and strain before failure. Concerning the zone (I), nanoparticle decoration endows PCL scaffolds with impressive stiffness, with increments up to 1575%. It is relevant to note that CNT-coating improves stiffness (1388%) at the expense of ductility (65% maximum strain), while GO-coating ensures good ductility retention (90%), while inducing lower enhancement of elastic modulus (ca. 1250%). Remarkably, the hybrid coating of GO and CNTs led to strong yet tough scaffolds, with 1575% stiffness improvement and 85-90% strain retention. Even in the densification region, GO-CNT@PCL, benefiting from the synergistic effect of GO-CNTs framework, experienced the highest elastic modulus and a dramatically higher compressive strength at the end of experiment, which reached the unprecedented value of 132 MPa, i.e., more than three orders of magnitude higher than those of graphene aerogels [15].

Table 3. Salient mechanical properties measured in the three representative zones

Sample	Zone I		Zone II		Zone III			
	E_I (MPa)	$(E_c/E_m)_I$	$\varepsilon_{Y,II}$ (%)	$\sigma_{Y,II}$ (MPa)	E_{III} (MPa)	$(E_c/E_m)_{III}$	$\varepsilon_{max,III}$ (%)	$\sigma_{max,III}$ (MPa)
PCL	0.16 ± 0.0	1	93 ± 1.5	9.6 ± 0.5	685 ± 14	1	99.1 ± 0.8	80 ± 2
GO@PCL	1.99 ± 0.0	12.44	81 ± 1.4	9 ± 0.2	893 ± 6	1.32	90.1 ± 3.3	58 ± 4
CNT@PCL	2.22 ± 0.6	13.88	55 ± 1.2	5 ± 0.1	2087 ± 7	3.09	65 ± 2.0	131± 2
GO-CNT@PCL	2.52 ± 0.2	15.75	78 ± 1.3	11 ±0.4	2998 ± 12	4.44	86 ± 4.0	132±1

Notably, GO-CNT@PCL retains excellent mechanical performance even in wet conditions, whereas the other materials experienced a slight decrease of all the mechanical properties (see **Fig. S6** and **Tab. S2**).

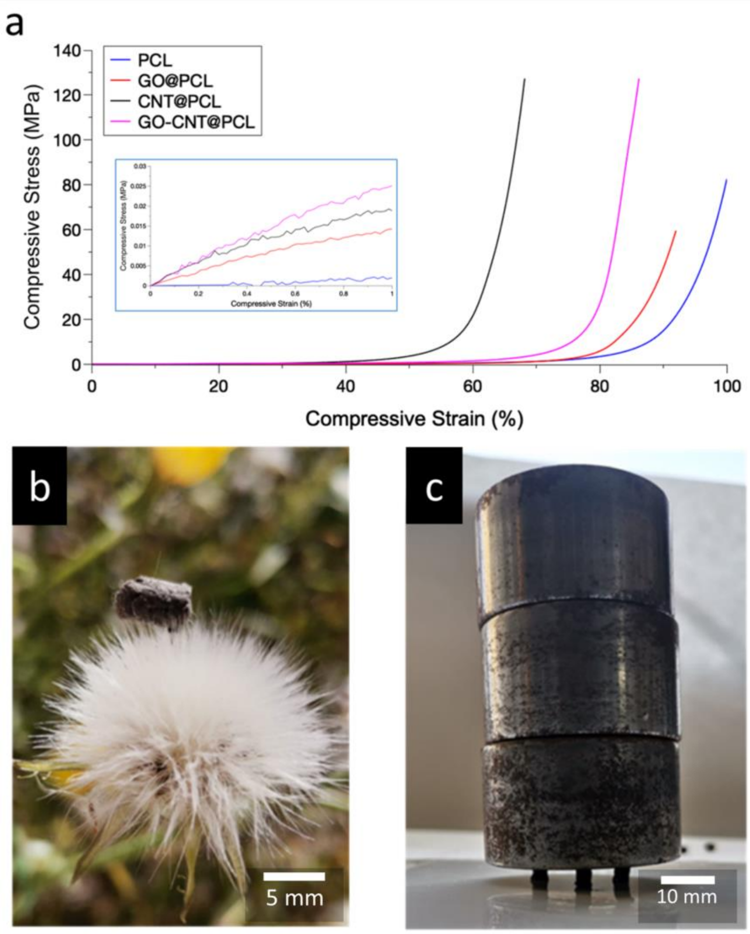

Figure 5. Representative stress-strain curves during compression tests (A), digital photographs of a GO-CNT@PCL scaffold on a dandelion (B), three GO-CNT@PCL scaffolds robust enough to withstand a compressive load of 0.6 kg (C).

Taken together, these findings outline that GO-CNT@PCL scaffolds are lightweight yet strong and tough materials, due to the unique combination of high porosity levels and mechanical robustness, as visually illustrated in the digital photographs of **Figure 5** b-c, where three GO-CNT@PCL scaffolds are strong enough to resist under a load of 0.6 kg and lightweight enough to preserve the structure of a dandelion.

The effect of the different architecture and surface chemistry on the surface wettability of such scaffolds was studied by WCA testing. **Figure 6** shows the behaviour of WCA as a function of time. Expectedly, PCL and CNT@PCL fluffy scaffolds displayed hydrophobic character, with WCA values above 100° in the whole experimental time, due to the hydrophobicity of substrate (especially in the presence of CNTs brushes) that hindered the water adsorption despite the porosity of the structure (see photographs and schematics in panels b-c). By contrast, GO@PCL sample, relying on the uniform GO-coating, showed remarkable hydrophilicity with water drops rapidly absorbed onto surface within 8-10 seconds. This feature could reasonably be ascribed to the synergistic effect of hydrophilic character of substrate (note that initial WCA is 50°) and porous architecture, as pictorially schematized in panel c, with positive repercussions on both surface roughness filling and bulk penetration, i.e., the two independent phenomena occurring in the imbibition of porous structures [40]. Notably, WCA of GO-CNT@PCL proved to decrease from 100° to 0° within one minute ca. This time-dependent switch from hydrophobic to hydrophilic character can be reasonably ascribed to the unique features of hierarchical, spider leg-like structure of these latter samples. In fact, at the beginning of the experiment, as the water drops meet CNT brushes, WCA is 100°, while progressively decreasing thereafter. Indeed, it was reported that time-dependence in WCA measurement generally indicates the coexistence of hydrophilic and hydrophobic domains that leads to the surface reconstruction when water drops are deposited on surfaces. The starting value was contributed by the hydrophobic component on coated-polymer surface and the equilibrium contact angle mainly by the hydrophilic components [41]. The WCA curve shows a change of concavity at ca. 10 s, thus likely suggesting that spreading and capillarity phenomena cooperate during water absorption, which is delayed by the presence of hydrophobic brushes (see Fig. 6c). This aspect is of enormous importance in the view of fabricating materials for the removal of pollutants from aqueous environment, since each single fibre of these scaffolds could be regarded as a nanopatterned environment, in which GO lamellae wrapped onto PCL fibres behave as wettable nanoplatforms for water molecules transfer, and CNT brushes can act as pollutant receptors, providing additional surface area and active sites.

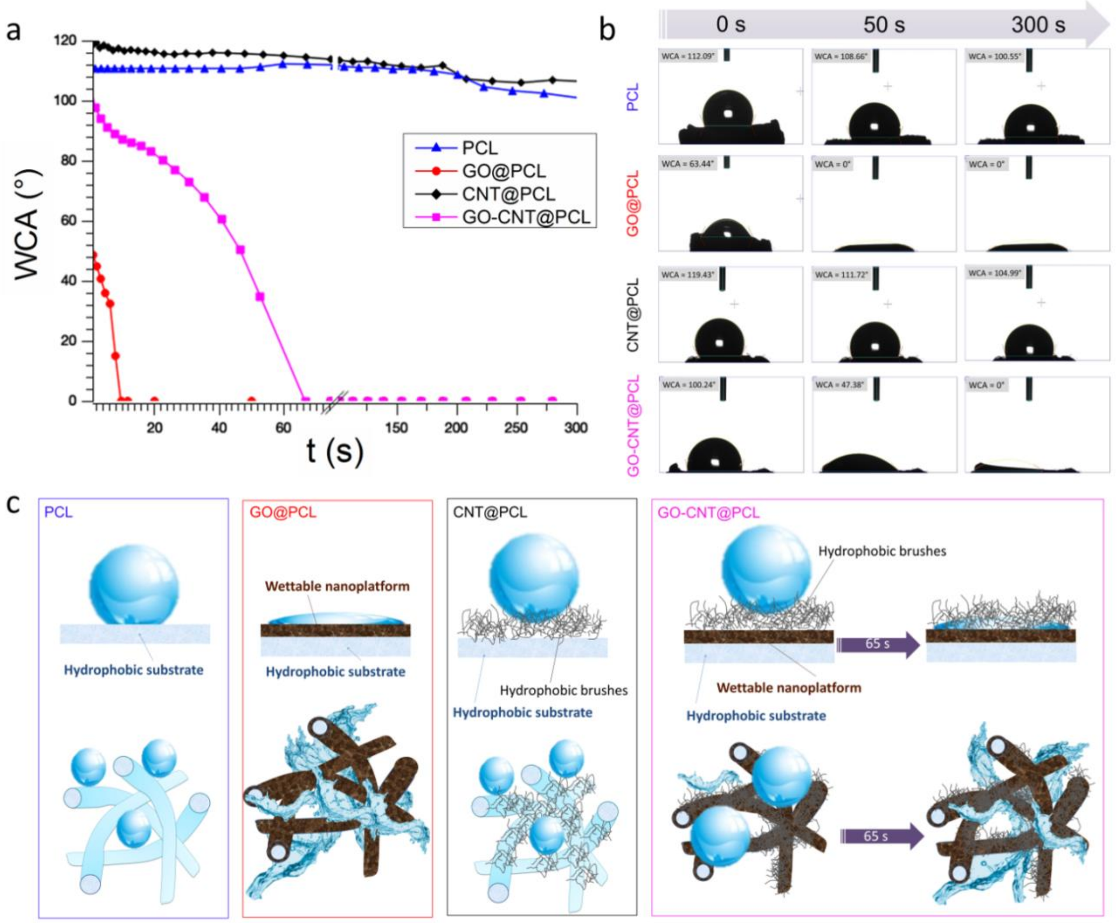

Figure 6. Wettability of the systems investigated. a) Time-dependent evolution of WCA; b) photographs taken at 0, 50, and 300 s; c) pictorial description of the possible mechanisms involving the characteristics of substrate (top) and fibrous architecture (bottom).

Hence, we investigated the effect of surface chemistry of fluffy scaffolds on their sorption performance towards two water soluble organic salts that show strong physicochemical stability, namely MB and MO. The former one is a cationic molecule used as a medication and dye. When used in huge amounts in the textile industry, the resulting wastewater becomes harmful to humans, thus causing skin, eye, and kidney diseases, beyond the obvious spoilage of water resources [42,43]. MO is an anionic azo dye that may cause significant biological and physiological alterations, with proven allergic, mutagenic, and carcinogenic effects to humans and fishes [44]. **Figure 7** shows the effect of contact time on the adsorption of MB and MO, assessed by monitoring the progressive decay of the characteristic UV absorption peaks in the solutions treated with GO@PCL (panel a, a'), CNT@PCL (b, b') and GO-CNT@PCL (c, c'), along with the digital photographs of solutions taken at the beginning and at the end of experiments for each sample. Sorption capacities and final removal efficiencies of all the systems investigated are displayed in **Figure 8**. First, the results point out that all the sorption curves, regardless of adsorbate-adsorbent system investigated, exhibit an initial, rapid adsorption, followed by a progressive plateauing. In the case of MB removal, all the materials display excellent performance, given the fact that such cationic salt is able to interact with both aromatic and oxygenated domains. Among them, GO@PCL reached the plateau more quickly than the other samples (within 350 min instead of 540 min), with 370 mg/g sorption capacity and 95% removal efficiency (the same values reported by CNT@PCL). GO-CNT@PCL performed better than the other samples with 400 mg/g sorption capacity and removal efficiency close to 100%. MO dye removal tests put into evidence the low performance of GO@PCL and CNT@PCL (less than 40% efficiency), albeit strong differences were observed in the shape of curves: extremely hydrophilic GO@PCL reached the plateau within 100 minutes, while hydrophobic CNT@PCL achieved the sorption equilibrium above 500 minutes. Interestingly, GO-CNT@PCL displayed 100% efficiency with more than 80 mg/g adsorbed within 6 hours, presumably benefiting from the combination of wettability, offered by GO, and abundance of active sites provided by CNTs. The synergistic effect of such hybrid framework was effective in achieving performance higher than the sum of the other two. In fact, in the case of water-soluble aromatic anionic dyes, nanocarbons can interact via π-π stacking only. In this sense, the few aromatic domains that GO retains after its oxidation (ca. 20% [45]) are the only active sites available for sorption, whereas the plenty of oxygenated moieties, while granting sufficient wettability and hence fast adsorption, are not suitable for interacting with negative MO because of obvious electrostatic repulsion. Therefore, GO@PCL displayed a fast sorption with extremely low removal efficiency. Otherwise, the extended sp^2-conjugated framework of CNT@PCL makes it suitable for MO complexation but, at the same time, remarkably hydrophobic. Consequently, in a stagnant flow regime, the bulk penetration of the aqueous solution is strongly hindered, thus representing the bottleneck of the sorption process. In both cases, although for different reasons, GO- and CNT-coatings were found to be ineffective in removing MO, while their combination into hybridized hierarchical structures generated unexpected and fascinating features. The feasibility of treating water contaminated by multiple dyes was explored by immersing GO-CNT@PCL samples in an aqueous solution containing both 0.5 mmol/L of MB and 0.1 mmol/L of MO. The results, showed in **Figure 9**, provide strong evidence that such materials are capable of adsorbing both pollutants. This behaviour could be reasonably explained by hypothesizing that the peculiar, hierarchical topochemistry of surface could have promoted the partitioning of MB and MO dyes, with the former preferentially and rapidly adsorbed onto hydrophilic domains of GO (note that MB is completely adsorbed within 3 hours), and the latter molecules mainly adsorbed onto sidewalls of CNT brushes, whose poor wettability resulted in slower kinetics.

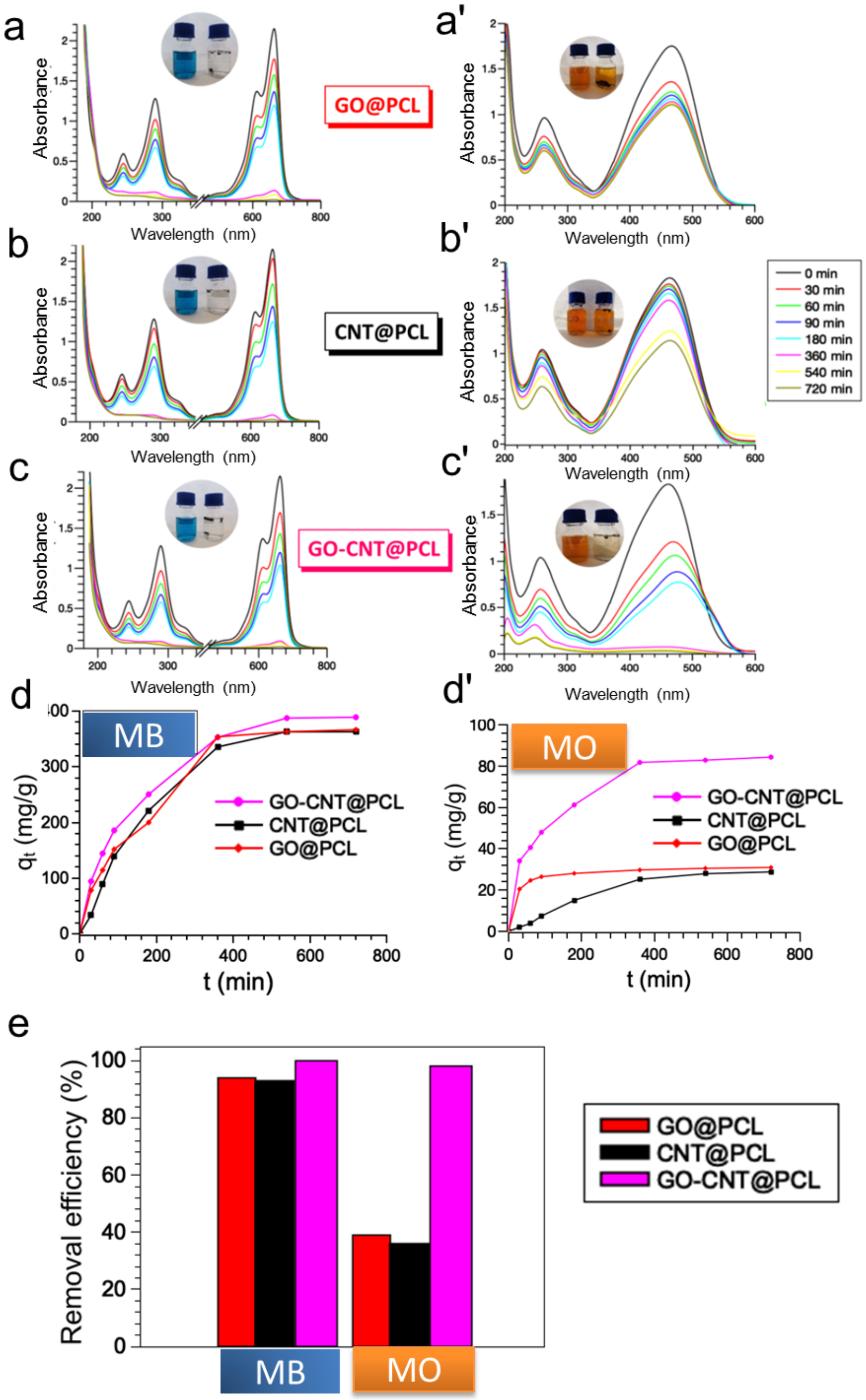

Figure 7. UV-vis spectra of MB (left) and MO (right) solutions treated with GO@PCL (a-a'), CNT@PCL (b-b') and GO-CNT@PCL (c-c') at different time intervals, along with digital photographs of solutions before and after experiments; adsorption of MB (d) and MO (d') upon time expressed as mg of pollutant per grams of sorbent systems; removal efficiency at the end of the experiment (c).

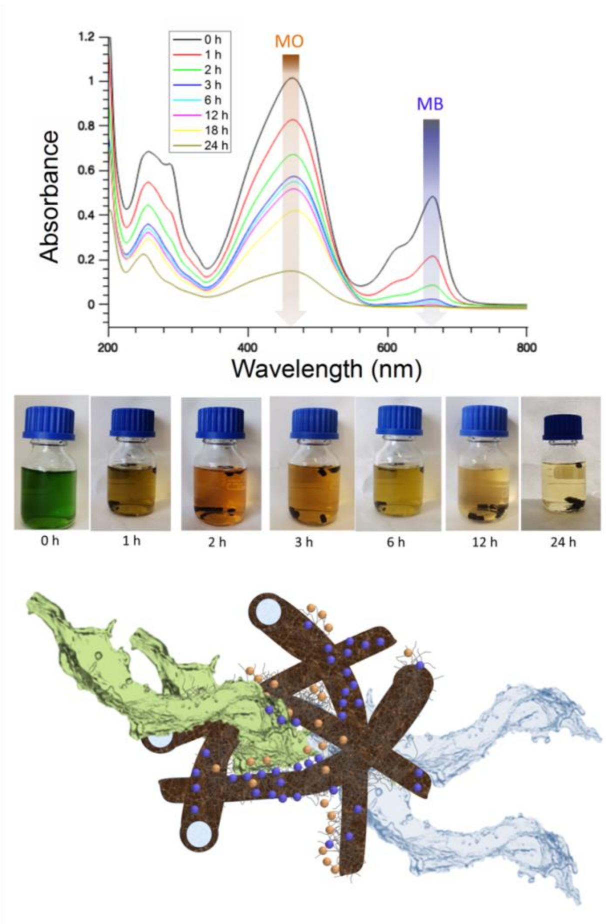

Figure 8. Decontamination of water from MB-MO mixture: digital photographs, UV-vis spectra, and pictorial representation of the possible mechanism.

Ultimately, **Tab. S3** provides a comparison between the results carried out in this work and those of other systems proposed for removal of MB and/or MO in similar conditions (i.e. similar mass to volume ratio, initial concentration of pollutants, neutral pH, and so on). Although only few papers report on the possibility to simultaneously recover anionic and cationic dyes, while there is a lot of literature investigating on the removal of solely MB or MO dyes, it can be seen that GO-CNT@PCL scaffolds prepared in this work perform much better than other relevant core-shell membranes and worse than GO-CNT aerogels prepared by in situ growth of CNTs onto GO 3D networks. However, compared to the latter, but also to all other systems, the mechanical robustness of GO-CNT@PCL fluffy scaffolds is three orders of magnitude higher and, to the best of our knowledge, our method is the fastest.

4. Conclusions

We demonstrated the feasibility of preparing core-shell fluffy scaffolds with tailored surface chemistry and spider-leg architecture, which can be exploited as broad-spectrum sorbents. A robust map of processing-structure-properties relationships was outlined, and it was elucidated the crucial role of GO as a building block for promoting CNTs decoration of PCL fibrous monoliths. In fact, GO is able to roll up around PCL fibers through electrostatic-aided wrapping, while attracting CNTs via π-π stacking. The resulting hierarchical structure comprises a flexible skeleton of PCL fibers wrapped by GO lamellae that behave as wettable nanoplatforms for water molecules fast diffusion, and CNT brushes that provide additional surface area and highly conjugated active sites. Such hierarchical architecture offers several advantages and outstanding versatility, enabling us to design materials with time-dependent wettability, capable of removing two different polar dyes and their combination. The porosity levels attained (96-99%) endow lightweight structures with extended surface area, while the outer GO-CNT framework allows stiffness increments up to 1575%, while retaining excellent toughness. Ultimately, such materials proved to display mechanical robustness more than 3 orders of magnitude higher than that of graphene aerogels, while displaying easy handling and removal from water, thus avoiding the risk of secondary pollution. Moreover, to strengthen the importance of having hierarchical structures equipped with wettable nanoplatforms, sorption tests were performed in the total absence of stirring, thus demonstrating the exceptional performance of such materials in removing both anionic and cationic dyes with efficiency close to 100% even in stagnant flow.

Acknowledgements

Work fully supported by PO-FESR-2014-2020-SICILIA, SAWE, “Support, Alerting, Early Warning” cod. no. 08PA9511000101 CUP G78I18000960007 Azione 1.1.5 Regione Siciliana.

References

[1] T. Fujioka, M.T.T. Ngo, R. Makabe, T. Ueyama, H. Takeuchi, T.T.V. Nga, et al., Submerged nanofiltration without pre-treatment for direct advanced drinking water treatment, Chemosphere. 265 (2021) 129056. doi:https://doi.org/10.1016/j.chemosphere.2020.129056.

[2] Y. Lin, Y. Tian, H. Sun, T. Hagio, Progress in modifications of 3D graphene-based adsorbents for environmental applications, Chemosphere. 270 (2021) 129420. doi:https://doi.org/10.1016/j.chemosphere.2020.129420.

[3] S. Ramalingam, A. Subramania, Effective Removal of Nitrates from the Drinking Water by Chemical and Electrochemical Methods , Eng. Sci. . 15 (2021) 80–88. doi:10.30919/es8d456 .

[4] M. Danish, M. Qamar, M.H. Suliman, M. Muneer, Photoelectrochemical and photocatalytic properties of Fe@ZnSQDs/TiO2 nanocomposites for degradation of different chromophoric organic pollutants in aqueous suspension, Adv. Compos. Hybrid Mater. 3 (2020) 570–582. doi:10.1007/s42114-020-00187-9.

[5] U.A. Dar, S. Salunke-Gawali, D. Shinde, S. Bhand, S. Satpute, Thermal and spectral studies of transition metal complexes of 2-bromo-3-hydroxynaphthalene-1,4-dione: Evaluation of antibacterial activity against six bacterial strains, Eng. Sci. 15 (2021) 105–115. doi:10.30919/es8d492.

[6] G. Aggrwal, S. Salunke-Gawali, S.P. Gejji, M. Nikalje, D. Chakravarty, P.L. Verma, et al., Reactions of 2, 3-dibromonaphthalene-1, 4-dione and pyridyl amines: X-ray structures, dft investigations, and selective detection of the hg2+ and ni2+ ions, Eng. Sci. 14 (2021) 78–93. doi:10.30919/es8d427.

[7] S.N. Patil, S.R. Prasad, An Impact of Nationwide Lockdown on Physico-chemical Parameters of Bhogavati River Water, ES Energy Environ. 11 (2021) 28–39. doi:10.30919/esee8c931.

[8] H. Liu, Y. Mao, Graphene Oxide-based Nanomaterials for Uranium Adsorptive Uptake , ES Mater. Manuf. . 13 (2021) 3–22. doi:10.30919/esmm5f453 .

[9] A. Maio, M. Gammino, E.F. Gulino, B. Megna, P. Fara, R. Scaffaro, Rapid One-Step Fabrication of Graphene Oxide-Decorated Polycaprolactone Three-Dimensional Templates for Water Treatment, ACS Appl. Polym. Mater. 2 (11) (2020) 4993–5005. doi:10.1021/acsapm.0c00852.

[10] S. Rojas, P. Horcajada, Metal–Organic Frameworks for the Removal of Emerging Organic Contaminants in Water, Chem. Rev. 120 (2020) 8378–8415. doi:10.1021/acs.chemrev.9b00797.

[11] Z. Sun, K. Qu, Y. Cheng, Y. You, Z. Huang, A. Umar, et al., Corncob-derived

Activated Carbon for Efficient Adsorption Dye in Sewage, ES Food Agrofor. 4 (2021) 61–73. doi:10.30919/esfaf473.

[12] P. Xie, Y. Liu, M. Feng, M. Niu, C. Liu, N. Wu, et al., Hierarchically porous Co/C nanocomposites for ultralight high-performance microwave absorption, Adv. Compos. Hybrid Mater. 4 (2021) 173–185. doi:10.1007/s42114-020-00202-z.

[13] N. Nidamanuri, Y. Li, Q. Li, M. Dong, Graphene and Graphene Oxide-Based Membranes for Gas Separation , Eng. Sci. . 9 (2020) 3–16. doi:10.30919/es8d128906 .

[14] B. Lee, S. Lee, M. Lee, D.H. Jeong, Y. Baek, J. Yoon, et al., Carbon nanotube-bonded graphene hybrid aerogels and their application to water purification, Nanoscale. 7 (2015) 6782–6789. doi:10.1039/c5nr01018g.

[15] L. Jiang, Y. Wen, Z. Zhu, X. Liu, W. Shao, A Double cross-linked strategy to construct graphene aerogels with highly efficient methylene blue adsorption performance, Chemosphere. 265 (2021). doi:10.1016/j.chemosphere.2020.129169.

[16] Y. Hua, F. Li, Y. Liu, G.-W. Huang, H.-M. Xiao, Y.-Q. Li, et al., Positive synergistic effect of graphene oxide/carbon nanotube hybrid coating on glass fiber/epoxy interfacial normal bond strength, Compos. Sci. Technol. 149 (2017) 294–304. doi:https://doi.org/10.1016/j.compscitech.2017.06.024.

[17] J. Wang, X. Jin, H. Wu, S. Guo, Polyimide reinforced with hybrid graphene oxide @ carbon nanotube: Toward high strength, toughness, electrical conductivity, Carbon N. Y. 123 (2017) 502–513. doi:https://doi.org/10.1016/j.carbon.2017.07.055.

[18] Z. Wang, H.-C. Yang, F. He, S. Peng, Y. Li, L. Shao, et al., Mussel-Inspired Surface Engineering for Water-Remediation Materials, Matter. 1 (2019) 115–155. doi:https://doi.org/10.1016/j.matt.2019.05.002.

[19] I. Bustero, I. Gaztelumendi, I. Obieta, M.A. Mendizabal, A. Zurutuza, A. Ortega, et al., Free-standing graphene films embedded in epoxy resin with enhanced thermal properties, Adv. Compos. Hybrid Mater. 3 (2020) 31–40. doi:10.1007/s42114-020-00136-6.

[20] N. Mohammad, Y. Atassi, Adsorption of methylene blue onto electrospun nanofibrous membranes of polylactic acid and polyacrylonitrile coated with chloride doped polyaniline, Sci. Rep. 10 (2020) 13412. doi:10.1038/s41598-020-69825-y.

[21] G. Qi, Y. Liu, L. Chen, P. Xie, D. Pan, Z. Shi, et al., Lightweight Fe3C@Fe/C nanocomposites derived from wasted cornstalks with high-efficiency microwave absorption and ultrathin thickness, Adv. Compos. Hybrid Mater. 4 (2021) 1226–1238. doi:10.1007/s42114-021-00368-0.

[22] C. Tang, G. Long, X. Hu, K.-W. Wong, W.-M. Lau, M. Fan, et al., Conductive polymer nanocomposites with hierarchical multi-scale structures via self-assembly of carbon-nanotubes on graphene on polymer-microspheres, Nanoscale. 6 (2014) 7877–7888. doi:10.1039/c3nr06056j.

[23] H. Lv, Y. Li, Z. Jia, L. Wang, X. Guo, B. Zhao, et al., Exceptionally porous three-dimensional architectural nanostructure derived from CNTs/graphene aerogel towards the ultra-wideband EM absorption, Compos. Part B Eng. 196 (2020) 108122. doi:https://doi.org/10.1016/j.compositesb.2020.108122.

[24] R. Scaffaro, A. Maio, Integrated ternary bionanocomposites with superior mechanical performance via the synergistic role of graphene and plasma treated carbon nanotubes, Compos. Part B Eng. (2019). doi:https://doi.org/10.1016/j.compositesb.2019.03.076.

[25] R. Scaffaro, A. Maio, G. Lo Re, A. Parisi, A. Busacca, Advanced piezoresistive sensor achieved by amphiphilic nanointerfaces of graphene oxide and biodegradable polymer blends, Compos. Sci. Technol. 156 (2018) 166–176. doi:https://doi.org/10.1016/j.compscitech.2018.01.008.

[26] A. Maio, R. Scaffaro, L. Lentini, A. Palumbo Piccionello, I. Pibiri, Perfluorocarbons–graphene oxide nanoplatforms as biocompatible oxygen reservoirs, Chem. Eng. J. 334 (2018) 54–65. doi:10.1016/j.cej.2017.10.032.

[27] A. Maio, L. Botta, A.C. Tito, L. Pellegrino, M. Daghetta, R. Scaffaro, Statistical study of the influence of CNTs purification and plasma functionalization on the properties of polycarbonate-CNTs nanocomposites, Plasma Process. Polym. 11 (2014). doi:10.1002/ppap.201400008.

[28] E. García-Hernández, C.G. Aguilar-Madera, E.C. Herrera-Hernández, R. Ocampo-Pérez, E. Bailón-García, F.B. Cortés, Hydrodynamic effects on the overall adsorption rate of phenol on activated carbon cloth through the advection-diffusion model application, J. Ind. Eng. Chem. 93 (2021) 267–278. doi:https://doi.org/10.1016/j.jiec.2020.10.003.

[29] K. Bubke, H. Gnewuch, M. Hempstead, J. Hammer, M.L.H. Green, Optical anisotropy of dispersed carbon nanotubes induced by an electric field, Appl. Phys. Lett. 71 (1997) 1906–1908. doi:10.1063/1.119976.

[30] F.V. Ferreira, W. Francisco, B.R.C. de Menezes, L.D.S. Cividanes, A. dos Reis Coutinho, G.P. Thim, Carbon nanotube functionalized with dodecylamine for the effective dispersion in solvents, Appl. Surf. Sci. 357 (2015) 2154–2159. doi:https://doi.org/10.1016/j.apsusc.2015.09.202.

[31] R. Scaffaro, A. Maio, F. Lopresti, D. Giallombardo, L. Botta, M.L. Bondì, et al., Synthesis and self-assembly of a PEGylated-graphene aerogel, Compos. Sci. Technol. 128 (2016) 193–200. doi:10.1016/j.compscitech.2016.03.030.

[32] A. Maio, S. Agnello, R. Khatibi, L. Botta, A. Alessi, A. Piazza, et al., A rapid and eco-friendly route to synthesize graphene-doped silica nanohybrids, J. Alloys Compd. 664 (2016) 428–438. doi:10.1016/j.jallcom.2015.12.137.

[33] S. Agnello, A. Alessi, G. Buscarino, A. Piazza, A. Maio, L. Botta, et al., Structural and thermal stability of graphene oxide-silica nanoparticles nanocomposites, J. Alloys Compd. 695 (2017) 2054–2064. doi:http://dx.doi.org/10.1016/j.jallcom.2016.11.044.

[34] A. Maio, D. Giallombardo, R. Scaffaro, A. Palumbo Piccionello, I. Pibiri, Synthesis of a fluorinated graphene oxide-silica nanohybrid: Improving oxygen affinity, RSC Adv. 6 (2016) 46037–46047. doi:10.1039/c6ra02585d.

[35] S. Claramunt, A. Varea, D. López-Díaz, M.M. Velázquez, A. Cornet, A. Cirera, The Importance of Interbands on the Interpretation of the Raman Spectrum of Graphene Oxide, J. Phys. Chem. C. 119 (2015) 10123–10129. doi:10.1021/acs.jpcc.5b01590.

[36] S.L.H. Rebelo, A. Guedes, M.E. Szefczyk, A.M. Pereira, J.P. Araújo, C. Freire, Progress in the Raman spectra analysis of covalently functionalized multiwalled carbon nanotubes: unraveling disorder in graphitic materials, Phys. Chem. Chem. Phys. 18 (2016) 12784–12796. doi:10.1039/C5CP06519D.

[37] A. Kołodziej, E. Długoń, M. Świętek, M. Ziąbka, E. Dawiec, M. Gubernat, et al., A raman spectroscopic analysis of polymer membranes with graphene oxide and reduced graphene oxide, J. Compos. Sci. 5 (2021). doi:10.3390/jcs5010020.

[38] E. Dervishi, Z. Ji, H. Htoon, M. Sykora, S.K. Doorn, Raman spectroscopy of bottom-up synthesized graphene quantum dots: size and structure dependence, Nanoscale. 11 (2019) 16571–16581. doi:10.1039/C9NR05345J.

[39] M. Gijare, S. Chaudhari, S. Ekar, A. Garje, Reduced Graphene Oxide Based Electrochemical Nonenzymatic Human Serum Glucose Sensor , ES Mater. Manuf. . 14 (2021) 110–119. doi:10.30919/esmm5f486 .

[40] S. Krainer, U. Hirn, Contact angle measurement on porous substrates: Effect of liquid absorption and drop size, Colloids Surfaces A Physicochem. Eng. Asp. 619 (2021) 126503. doi:https://doi.org/10.1016/j.colsurfa.2021.126503.

[41] X. Wang, Z. Chen, Z. Shen, Dynamic behavior of polymer surface and the time dependence of contact angle, Sci. China Ser. B Chem. 48 (2005) 553–559. doi:10.1360/042004-22.

[42] M. Aravind, A. Ahmad, I. Ahmad, M. Amalanathan, K. Naseem, S.M.M. Mary, et al., Critical green routing synthesis of silver NPs using jasmine flower extract for biological activities and photocatalytical degradation of methylene blue, J. Environ. Chem. Eng. 9 (2021). doi:10.1016/j.jece.2020.104877.

[43] M. Adeel, M. Saeed, I. Khan, M. Muneer, N. Akram, Synthesis and Characterization of Co-ZnO and Evaluation of Its Photocatalytic Activity for Photodegradation of Methyl Orange, ACS Omega. 6 (2021) 1426–1435. doi:10.1021/acsomega.0c05092.

[44] M. Alaguprathana, M. Poonkothai, Haematological, biochemical, enzymological and histological responses of Labeo rohita exposed to methyl orange dye solution treated with Oedogonium subplagiostomum AP1, Environ. Sci. Pollut. Res. 28 (2021) 17602–17612. doi:10.1007/s11356-020-12208-7.

[45] R. Scaffaro, A. Maio, A green method to prepare nanosilica modified graphene oxide to inhibit nanoparticles re-aggregation during melt processing, Chem. Eng. J. 308 (2017) 1034–1047. doi:10.1016/j.cej.2016.09.131.